Supporting Information

Probing the Birth and Ultrafast Dynamics of Hydrated Electrons at the Gold/Liquid Water Interface *via* an Optoelectronic Approach

François Lapointe[1,2], Martin Wolf[1], R. Kramer Campen[1,3], Yujin Tong[1,3,*]

Affiliations

1. Fritz Haber Institute of the Max Planck Society, Faradayweg 4-6, 14195 Berlin, Germany
2. Now at: National Research Council Canada, 1200 Montreal Road, Ottawa, Ontario K1A 0R6, Canada
3. Faculty of Physics, University of Duisburg-Essen, Lotharstrasse 1, 47057 Duisburg, Germany

* Correspondence author: tong@fhi-berlin.mpg.de

Contents

S-1 Experimental principles

This optoelectronic technique to probe the electrode-electrolyte interface combines optical perturbation of the system with coulostatic measurements. As described by Richardson *et al.*, "coulostatic" measurements consist of a perturbation of the electrode-electrolyte interface by an instantaneous pulse of charges,[1] followed by monitoring the working electrode (WE) potential in the open circuit potential (OCP) mode of the potentiostat instrument.

Two pulsed beams spatially overlap at the electrode/electrolyte interface while the time averaged photovoltage is continuously monitored with a potentiostat. As the shutter of the first pump beam [ultraviolet (UV), 267 nm, $\sim$110 fs] is opened [Fig. S1(a)], carriers are photoexcited in the continuum of electronic states in the metallic electrode, and a portion of the carriers are ejected to the conduction band of water[2]. The combined effect of heat generated at the electrode and photoinjection of carriers to the solution induces a large potential jump ΔV_1 on the order of 200–300 mV [inset of Fig. S1(b)].[1,3,4] The introduction of the second pump creates a second photovoltage ΔV_2 only if both pulses match certain delay conditions that are photon energy-dependent. There is no measurable photovoltage change for completely detuned pulses. Hence, the second pump will interact only with hydrated electrons and precursor states [see Fig. 1(a), main text]. The excess electrons at the interface create a supplemental channel for

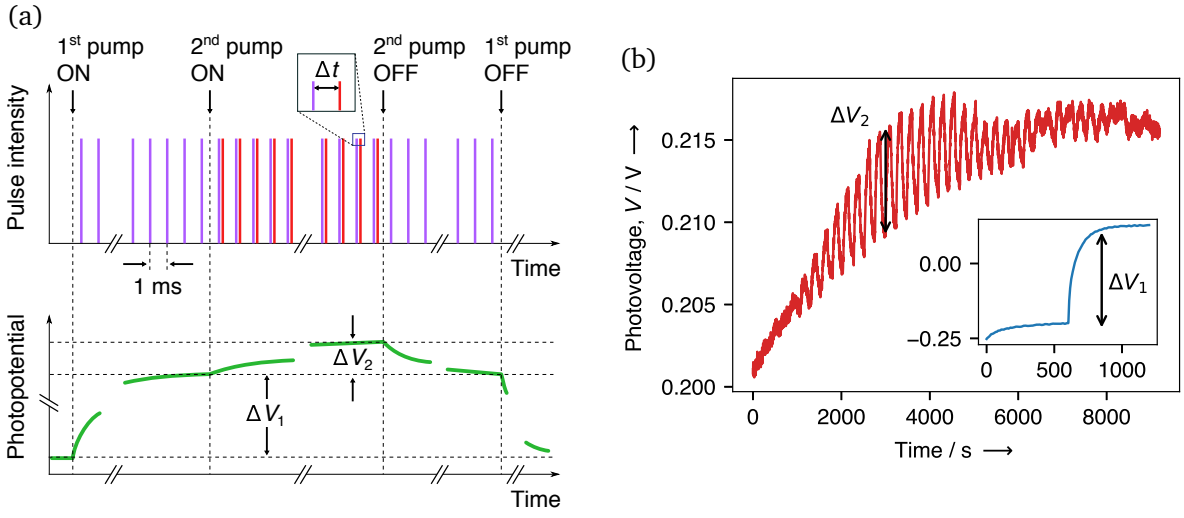

Figure S1: (a) Sequence of pulses for the two pump beams and their effect on the photovoltage represented conceptually. (b) Experimental data of the photovoltage jumps ΔV_2 caused by the second pump beam for various delay values. Inset: Photovoltage jump ΔV_1 caused by the UV pump beam alone.

photon absorption and their subsequent relaxation back to ground state generates a temperature difference by releasing heat at the interface. It needs to be emphasized that the ultrafast process that induces the second photovoltage is decoupled from the slow kinetics at the metal/solution interface, hence an ultrafast time resolution can be achieved even though the electrochemical equilibrium takes place on a minute time scale. It is worth noting that, while the absorption of the second photon by the transient species takes place on an ultrafast time scale, collecting a single delay point is a long process (typically, 1 min. 2nd pump off and 1 min. 2nd pump on), which is fully consistent with the fact that heat diffusion is slow and that a very small temperature difference is building up. From there, it is well established that a temperature difference between the working (elevated temperature) and the reference (room temperature) electrodes transduces into a potential difference,[3] which is how the second photovoltage ΔV_2 is created. The different states of the solvated electron can then be identified by changing the photon energy of the second pulse and their delays.

A potentiostatic variant of the two-pulse technique was used to report on the picosecond dynamics of photoelectrons in hexane.[5] The detection scheme used by Scott was also different: A fast high voltage pulse (2 kV) moved the electrons out from the sample interface to the sensor electrode, 4 mm away.

The electrical double layer (EDL) acts as a capacitor with $Q = CV$, where Q is the charge, C is the capacitance of the EDL and V is the voltage. The presence of uncompensated charges in the EDL thus results in a photovoltage. At a concentration of 0.5 M Na_2SO_4 in water, the Debye length λ_D is $\sim$2.5 Å, meaning that we are only probing the charged species located closer than circa two bond lengths from the surface.

As noted above, a voltage can also be established by creating a temperature difference between electrodes. The temperature dependence of the voltage has been exploited previously in temperature jump measurements.[3,6,7] The total photovoltage due to heating of the metal-solution boundary is the sum of the internal drop of potential at the metal-solution boundary V_i, of the thermodiffusion potential of the solution (Soret effect) V_S, and of the thermal EMF of the metal V_{EMF}, such that $V = V_i + V_S + V_{EMF}$. The contribution of V_{EMF} is negligible in comparison to V_i, but the Soret effect V_S, while typically much smaller than V_i, can be important, depending on the electrolyte nature and pH.[3] As shown below (§ S-3 and § S-5.4) using the two-temperature model,

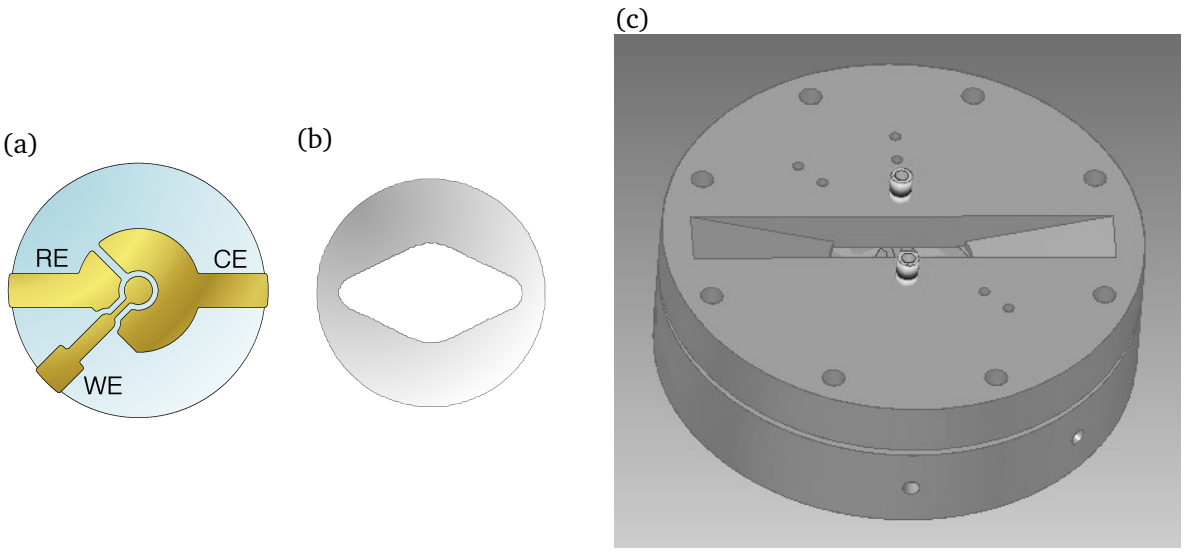

Figure S2: (a) Set of polycrystalline gold electrodes on a quartz plate fabricated by electron beam evaporation. (b) Shape of the 50 μm thick PTFE spacer used to defined the inner chamber of the spectroelectrochemical cell yielding a volume of ∼6 μL. (b) The cell assembly showing the aperture for the laser beams, and the inlet / outlet for flowing the electrolyte.

heating resulting from an ultrafast pulse can yield, in gold, a transient electronic temperature T_e as high as 1750 K, which results to an increase of the lattice temperature T_l on the order of 15 K.

S-2 Methodology

S-2.1 Spectroelectrochemical cell

The spectroelectrochemical cell (SEC) consists of a set of 3 gold electrodes (5 nm Cr / 200 nm Au) deposited through electron beam deposition on top of a quartz plate ($\varphi = 45$ mm) [Fig. S2(a)], thus defining the working, reference and counter electrodes (WE, RE and CE, respectively). The WE is a disk of 5 mm diameter at the center of the plate (effective area: 30.8 mm^2). The CE is larger in area, totalling 51.5 mm^2, while the metallic RE (effective area: 10 mm^2) provides a pseudo-reference. The gap between the WE and the CE is 1 mm and so is the gap between the WE and the RE. The gap between the RE and the CE is 1.5 mm. The cell is closed by capping with a CaF_2 window [diameter 25 mm, thickness 3 mm, UV grade, Global Optics (UK) Ltd], drilled through with two holes to allow the flow of the electrolyte, and separated by a 50 μm PTFE spacer cut in the shape shown in Fig. S2(b), using the assembly displayed in Fig. S2(c). Copper foil is used to electrically contact the electrodes externally.

The electrolyte consists of Na_2SO_4 in deionized water (18.2 MΩ· cm, Millipore) at a concentration of 0.5 M. It is deaerated by bubbling dry N_2 in the reservoir for at least 30 min. before the measurement is started. The flow of the electrolyte is assured by a peristaltic pump at a rate of 6 μL / s. In order to avoid any spurious effect by species generated at the CE, the electrolyte inlet is located above the RE and the outlet above the CE.

S-2.2 Electrochemical measurements

A potentiostat (VSP, Bio-Logic Science Instruments) was employed to record the open circuit potential (OCP). It was found useful, before the coulostatic measurements, to "clean" the WE by performing a series of cyclic voltammetry (CV) sweeps until the CV data showed the appropriate profile for a polycrystalline gold electrode in a thin film configuration. The RE would be cleaned in a similar manner whenever the drift was becoming important.

S-2.3 Laser setup

The layout of the laser system that was employed in this study is shown in [Fig. S3]. In brief, the laser system is composed of a Ti:Sapphire oscillator (Vitara, Coherent) and regenerative amplifier (Legend Elite Duo HE and Cryo PA, Coherent). One third of the amplifier output—7.0 mJ / pulse, 45 fs pulses, 1 kHz, centered at 800 nm—was used for the current experiment. 1 mJ / pulse of this output was used to feed the home-built optical tripler, from which the 267 nm and 400 nm photons were generated. A half-wave plate / polarizer / half-wave plate combination was used to adjust the energy of the 267 (400) nm beam at the sample. A typical value of ∼ 4 μJ / pulse and a lens with a 500 mm focal length were chosen for the experiments. Depending on the frequency, the second pump beam was either generated from difference frequency generation of Signal and Idler output from a commercial optical parametric amplifier (HE-TOPAS, Light Conversion), or used directly the Idler or Signal or double the frequency of the them.

Synchronization of the arrival of the pulses is necessary. For this purpose, we have used the bleaching by the UV pump of the nonlinear optical signal coming from the gold-electrolyte interface. The nonlinear optical signal $\omega_{NL} = \omega_1 + \omega_2$ stems from a nonresonant sum-frequency generation mixing a 800 nm ω_1 beam with the beam ω_2 also serving as a second pump. The bleaching of the optical nonlinear signal is coarsely correlated with the maximum of the

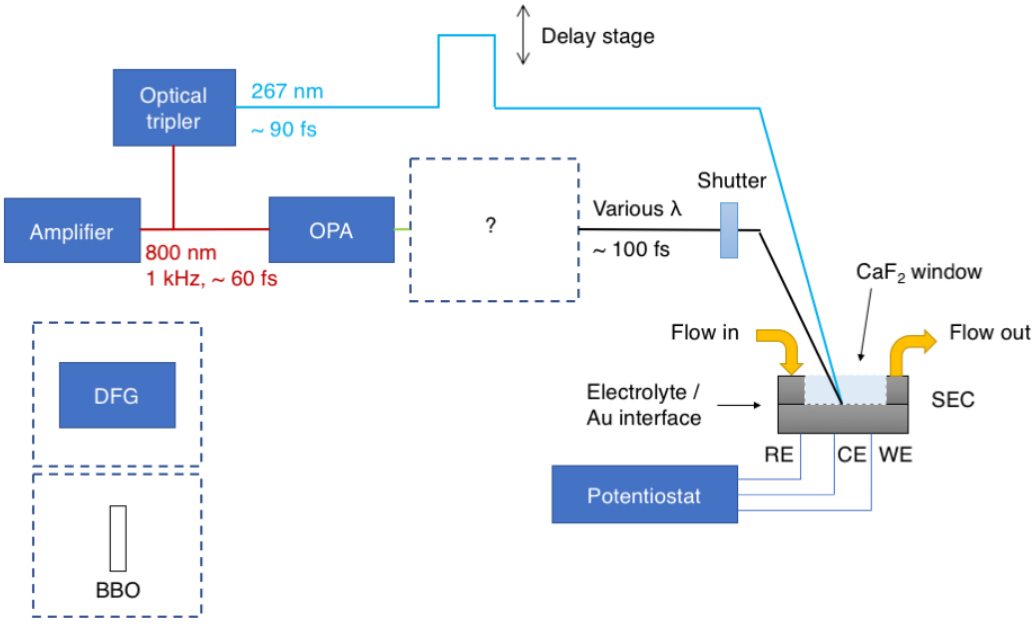

Figure S3: Diagram of the laser setup. The dashed boxed represent the elements that were interchanged as described in § S-2.3.1 to generate the various second pump wavelengths. From dispersion calculations presented in § S-2.6 and Fig. S4, the pulse width of the 267 nm beam is estimated to be ∼110 fs at the buried electrode (after transmission through a lens, windows and water layer.

photovoltage change due to the second pump pulse. The first pump delay stage is thus swept to find the maximal bleaching.

S-2.3.1 Generation of various wavelengths for the second pump's pulse

Various ultrashort pulses have been employed in this study as the second pump's pulses. They were generated as following:

670 and 720 nm The TOPAS' Signal outputs at 1340 and 1440 nm, respectively, were doubled in a BBO crystal and the fundamental beams were subsequently filtered out.

800 nm The 800 nm residual from the TOPAS after the parametric process was separated from the Idler and Signal beams and attenuated to required energy.

1000 nm The TOPAS' Idler output at 2000 nm was double in a BBO crystal and the fundamental beam was subsequently filtered out.

1333 and 2000 nm The TOPAS' Signal and Idler beams were directly taken at 1333 and 2000 nm, respectively.

4000 nm The TOPAS' Signal and Idler beams were mixed in the DFG crystal ($AgGaS_2$) in a noncollinear geometry. The Idler and Signal residuals were spatially filtered out.

S-2.4 Optoelectronic measurements

After the first pump beam shutter is opened, we let ΔV_1 reach an equilibrium value for approximately 10 min before the time delay series of the second pump beam is started. The shutter of the second pump beam is then sequentially opened and closed at 1 min intervals and the delay between the pulses of the first and second pumps is stepped at every repetition while photovoltage is continuously acquired in OCP mode. As can be seen in Fig. S1(b), every delay step corresponds to a spike of photovoltage ΔV_2 of varying amplitude reaching up to 10 mV. Maximum amplitude occurs in the vicinity of the zero time delay. The spikes are lost in the noise when the 2^{nd} pump pulses precede the 1^{st} pump (negative time delays) or when the beams are largely detuned. Whenever the UV pump beam is shut off, the second pump beam does not have any measurable effect on the photovoltage. Such series of delay steps is repeated for every energy of the second pump beam [0.31 (4000), 0.62 (2000), 0.93 (1333), 1.24 (1000), 1.55 (800), 1.72 (720) and 1.85 eV (670 nm)].

S-2.5 Data processing

The photovoltage change ΔV_2 due to the action of the second pump beam is first extracted in (post-measurement) data processing from the as-measured photovoltage versus elapsed experimental time [shown in Fig. S1(b)]. It is defined as the difference of the photovoltage measured when the second beam has been impinging for 1 min to the photovoltage measured after the second pump beam has been shut off for 1 min. Each photovoltage spike thus corresponds to a different delay of the first and second pump pulses. The photovoltage change is then corrected for the measured pulse energy of the first (P_1) and second pump (P_2) beams and the absorptivity of water at the wavelength of the second pump for a given angle θ of the second pump beam, a water layer thickness d_w and known water extinction coefficients α [8–10]. The effective water thickness d_w^{eff} is

Wavelength of 2nd pump (nm)	Photon energy (eV)	UV pulse energy (μJ)	2nd pulse energy (μJ)	Water abs. coeff. (cm^{-1})	Reference
670	1.85	5.3	4	0.00439	Pope and Fry [8]
720	1.72	5.3	4	0.01231	Pope and Fry [8]
800	1.55	5	8	0.02	Curcio and Petty [9]
1000	1.24	4	6	0.36	Curcio and Petty [9]
1333	0.93	4	5.1	1.4	Curcio and Petty [9]
2000	0.62	4	3.85	67	Curcio and Petty [9]
4000	0.31	5	4	170	Downing and Williams [10]

Table S1: Pulse energy for the first (UV) and second pumps, and the absorption coefficients of water at the second pump wavelength.

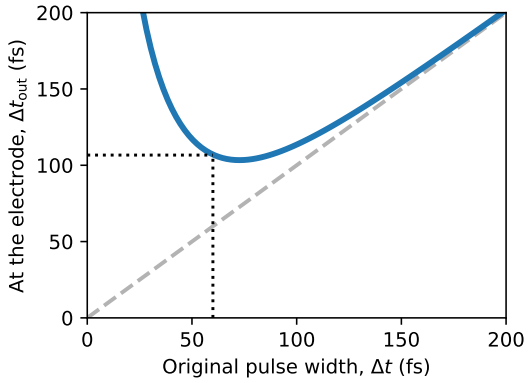

Figure S4: Broadening of the UV pulse after traversal of 15 mm CaF_2 lens, a 3 mm CaF_2 window and 50 μm of water.

calculated from Snell's law and the second pump incidence angle in air ($\theta_{air} = 0.95993$ rad) with $d_{CaF_2} = 3$ mm and wavelength-dependent n_{CaF_2} and n_w [11]. The different pulse energy values and water extinction coefficients are tabulated in Table S1. The correction to the raw photovoltage change ΔV_2^{raw} is expressed as:

$$\Delta V_2^{corr} = \Delta V_2^{raw} \left[P_1 P_2 \exp\left(-\alpha d_w^{eff}\right) \right]^{-1}. \tag{S1}$$

It is thus ΔV_2^{corr} that is presented in the main text as ΔV_2 for simplicity. Error on the data was estimated by propagation of the readout noise on ΔV_2^{raw} and the power fluctuation of the first and second pump laser beams P_1 and P_2.

S-2.6 Ultrafast pulse dispersion

The effect of CaF_2 optics (15 mm lens + 3 mm window) and water layer (50 μm) on the UV pulse duration (nominally 60 fs, 267 nm, at the amplifier's output) was calculated.[11–13] As seen in Fig. S4, the smallest pulse duration is ∼106 fs. Given that the output from the amplifier is ∼60 fs, that there should be no significant change of the pulse duration in the tripler, and that the curve shown in Fig. S4 is rather flat between 60 and 110 fs, a pulse FWHM of 110 fs for the UV light pulse duration is reasonable and will be used in data analysis and simulations.

S-3 Heating of the interface

Heating of the gold electrode has been simulated numerically using a two-temperature model (TTM) in Python 3.[14] The code was tested against the data and numerical simulations from Eesley *et al.* from nonequilibrium electron heating in copper[15].

We used a gold thickness of 200 nm, a thermal conductivity of 317 $W\,m^{-1}\,K^{-1}$ [16] and 1 $W\,m^{-1}\,K^{-1}$ for the electron and lattice systems, respectively, an electron heat capacity of $T_e \times 3.6 \times 10^{-3}\,J\,g^{-1}\,K^{-1}$ [16] and a lattice heat capacity of 0.129 $J\,g^{-1}\,K^{-1}$. Gold density was taken as 19.3 $g\,cm^{-3}$ and the electron-phonon coupling term was 2.2×10^{10} $W\,cm^{-3}\,K^{-1}$ [17]. For the laser pulse, we used a reflection coefficient (at 267 nm) of 0.35, a penetration depth of 11.9 nm, an energy density of 0.637×10^{-3} $J\,cm^{-2}$ and a pulse duration of 110 fs.

S-4 Models and fitting

S-4.1 Three-state model

Aiming to model the dynamics at the interface, we used a system of five coupled ordinary differential equations that are solved numerically to find the populations N_i at various states S_0 to S_4 in the system, of which 3 states are solution-side [Fig. 3(a)]:

$$\frac{dN_0}{dt'} = -I(t')N_0 + \frac{N_1}{\tau_{th}}, \tag{S2}$$

$$\frac{dN_1}{dt'} = I(t')N_0 - \frac{N_1}{\tau_{th}} - \frac{N_1}{\tau_0}, \tag{S3}$$

$$\frac{\mathrm{d}N_2}{\mathrm{d}t'} = \zeta \frac{N_1}{\tau_0} - \frac{N_2}{\tau_1}, \tag{S4}$$

$$\frac{\mathrm{d}N_3}{\mathrm{d}t'} = (1-\zeta) \frac{N_1}{\tau_0} + \frac{N_2}{\tau_1} - \frac{N_3}{\tau_2}, \tag{S5}$$

$$\frac{\mathrm{d}N_4}{\mathrm{d}t'} = \frac{N_3}{\tau_2} - \frac{N_4}{\tau_3}, \tag{S6}$$

where and $I(t)$ is the intensity of the time-dependent UV pump pulse. In order to correctly capture the dynamics of the shoulder feature in Fig. 1(d), where some amplitude appears early, we follow the concept used by Stähler *et al.* where a minority portion of the injected electrons reaches directly a trap state[18]. In equations S4 and S5, ζ is thus the ratio of electrons injected directly to the state S_2.

Assuming that only electron populations on the solution side contribute to the signal, the photovoltage change ΔV_2 is related to populations N_2, N_3 and N_4 through absorption coefficients a_i:

$$\Delta V_2 = a_2 N_2 + a_3 N_3 + a_4 N_4. \tag{S7}$$

Only four parameters are thus adjusted for every excitation energy: three absorption coefficients and a delay offset.

Metals dynamics have been taken into account in the model, even though it was found to be mostly insensitive to them: We have therefore lumped the metal-side thermalization into an effective relaxation time $\tau_{\mathrm{th}} = 1$ ps[19]. The characteristic times $\tau_0 = 0.12$ ps and $\tau_1 = 0.14$ ps, respectively assigned to injection and initial trapping, have been determined while fitting the fastest decay at an excitation energy of 0.31 eV. Considering that the excitation pulse width has been taken as 0.11 ps after calculation of the dispersion in the media it traverses, τ_0 and τ_1 values are likely to be limited by the experimental time resolution. Nonetheless, τ_1 can't possibly be much smaller than the excitation pulse width, otherwise the contribution from light absorption by state S_2 would not be observed. Finally, the characteristic time $\tau_2 = 0.82$ ps related to the final solvation step and the time $\tau_3 \simeq 51$ ps, encompassing the decay into products and the diffusion away from the EDL, have been extracted from the fit of the trace corresponding to an excitation energy of 1.85 eV. Time resolution is limited by the determination of time zero, which is lying within the convolution of the excitation (110 fs) and the second pulses (65 fs).

Back capture by the electrode [orange arrow in Fig. 3(a)] has not been explicitly implemented but it is expected to contribute to the effective characteristic times. As the back capture rate is higher for electrons of higher energy, the contribution should be more important for τ_0 and τ_1.

S-4.2 Two-state model

For the sake of comparison, we also implemented a simpler two-state model where the state S_3 is eliminated:

$$\frac{\mathrm{d}N_0}{\mathrm{d}t'} = -I(t')N_0 + \frac{N_1}{\tau_{\mathrm{th}}}, \tag{S8}$$

$$\frac{\mathrm{d}N_1}{\mathrm{d}t'} = I(t')N_0 - \frac{N_1}{\tau_{\mathrm{th}}} - \frac{N_1}{\tau_0}, \tag{S9}$$

$$\frac{\mathrm{d}N_2}{\mathrm{d}t'} = \zeta\frac{N_1}{\tau_0} - \frac{N_2}{\tau_1}, \tag{S10}$$

$$\frac{\mathrm{d}N_4}{\mathrm{d}t'} = \frac{N_2}{\tau_1} - \frac{N_4}{\tau_3}, \tag{S11}$$

and using:

$$\Delta V_2 = a_2 N_2 + a_4 N_4. \tag{S12}$$

Using this set of equations, we were unable to obtain a common set of characteristic times that correctly described the traces at every wavelengths. For instance, τ_3 remained fairly unaffected with a value of 52.1 ps. However, τ_1 was very much dependent on the second pump wavelength. Fitting the model at a second pump wavelength of 800 nm yielded a τ_1 with a value of 900 fs, while a fit at 4 μm gave a value of 110 fs. As can be attested in Fig. S6(a), a satisfying agreement at all second pump wavelengths cannot be reached with a model with only two states on the solution side.

S-5 Results

S-5.1 Characterization of the spectroelectrochemical cell

Figure S5 shows a cyclic voltammogram (CV) of the gold electrode in 0.5 M Na_2SO_4 aqueous solution collected with a scan rate of 1 mV/s in the spectroelectrochemical cell.

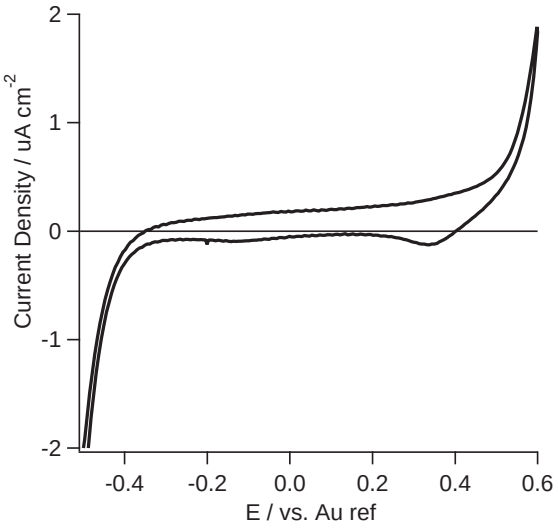

Figure S5: Cyclic voltammogram of the gold electrode in 0.5 M Na_2SO_4 in spectroelectrochemical cell (scanning speed 1 mV/s).

Table S2: Characteristic times used in the fitting of the three-state model.

τ_0	0.12 ps
τ_1	0.14 ps
τ_2	0.82 ps
τ_3	51.0 ps
UV pulse FWHM	0.11 ps

S-5.2 Time delay traces

The full set of time delay traces for various second pump energies is presented in Fig. S6. A zoom near the origin is shown for all energies in Fig. S6(a), while longer traces are displayed in (b) for energies 1.24 to 1.85 eV. The fit results (red dashed lines, computed as described in section S-4) are overlaid on the data (gray circles). As described in the main text, the photovoltage response ΔV_2 to the UV excitation (first pump) is highly dependent on the second pump wavelength. At low energies, the signal rise and decay is fast, on the order of 100 fs. As the second pump energy is increased, the signal persists for much longer, with residual intensity at 100 ps at 1.55 eV and above. We also note the large changes in peak ΔV_2. At 0.31 eV, the signal reaches approximately 0.18 mV, while the peak signal at 1.85 eV is more than 1000 times weaker.

In comparison to the best fit results obtained with a three-state model (red dashed line), the fit results from a two-state model are also shown on the same figures. Two cases are displayed,

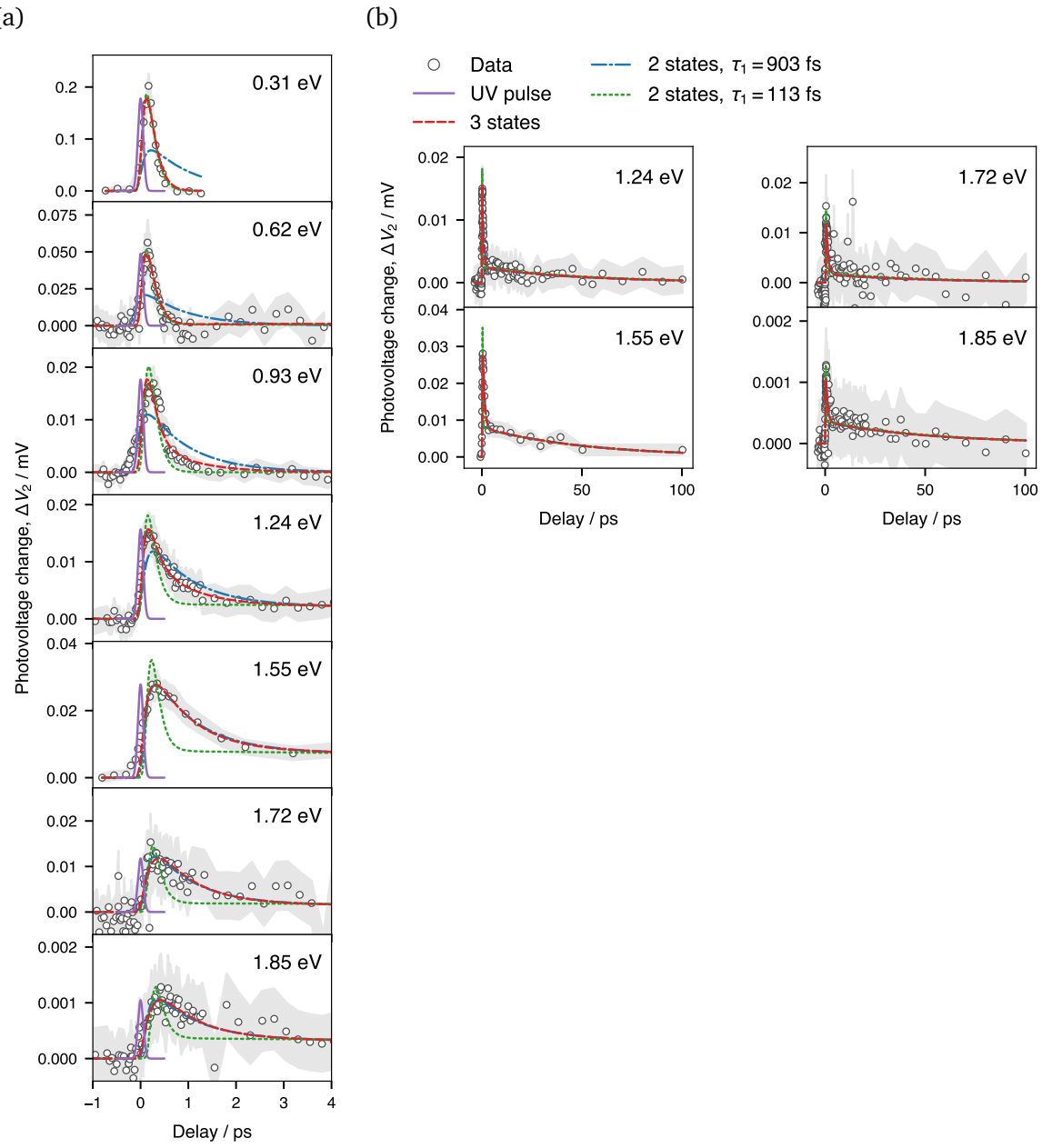

Figure S6: (a-b) The photovoltage change ΔV_2 versus the delay time. (a) At delays smaller than 4 ps. (b) At longer delays, up to 100 ps.

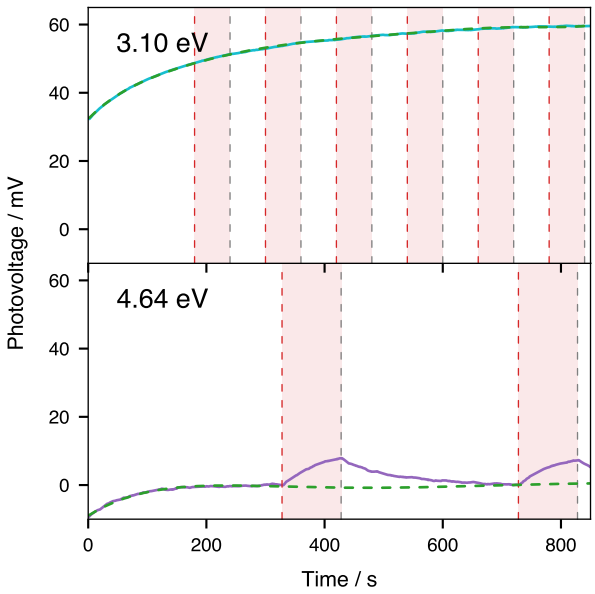

Figure S7: Comparison of the photovoltage when the first excitation pulse is changed from UV (4.64 eV, bottom) to blue (3.10 eV, top). The second pulse's energy is 0.31 eV in both cases. The red boxes show the times during which the shutter is open and the second pulse impinges on the electrode. The green dashed lines show the polynomial baseline subtracted to give the data shown in Fig. 1 of the main text.

where τ_1 has been determined from a fit at a second pump wavelength of 800 nm (blue dashed-dotted line) and 4 μm (green dotted line) as explained above. The discrepancy is most obvious at short delay times in Fig. S6(a).

S-5.3 Effect of the first pump energy

Fig. S7 compares on the same scale the untreated response to a 0.31 eV second pump for two different first pump energies: 3.10 eV (blue, top) and 4.64 eV (UV, bottom). Both traces display an initial drift, but settle to a different photovoltage. The red bands indicate when the second pump shutter is open, with a clear difference between the blue and UV first pumps. Indeed, for the blue first pump, the second pump shutter has a negligible effect on the signal, while a clear photovoltage increase is measured in the case of the UV first pump.

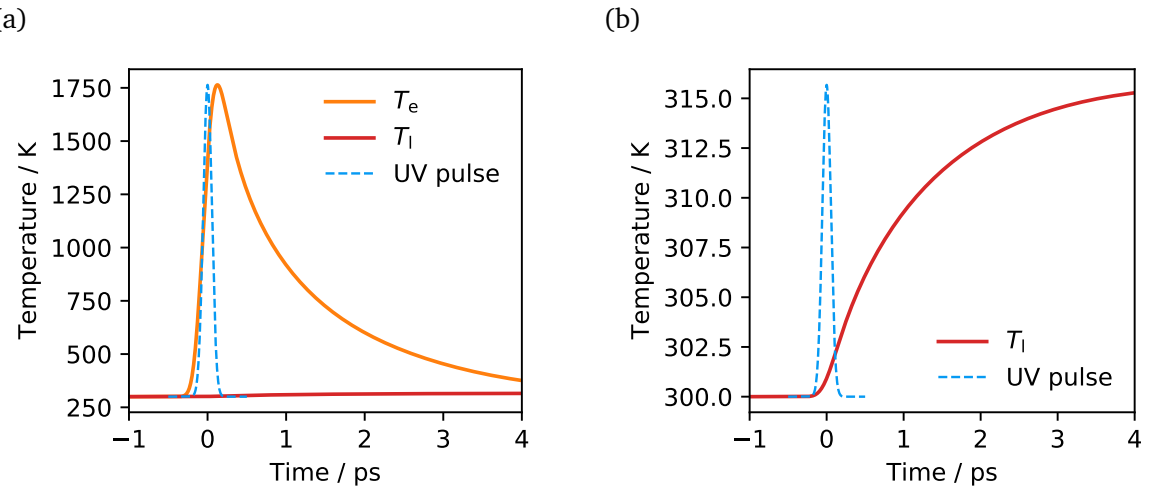

Figure S8: Electronic and lattice temperatures calculated from finite element analysis for an incoming UV pulse (267 nm) with 110 fs Gaussian FWHM and a peak power density of 5.79 × 10^9 W cm^2 on a 200 nm thick gold film. (a) Electronic and lattice temperatures. (b) Lattice temperature only.

S-5.4 Simulation of heating of the gold electrode surface by an ultrafast UV pulse

We have simulated the heating of the gold-water interface as described in § S-3 using the two-temperature model and calculated the temperature-related changes due to intraband and interband transitions. Results for both T_e and T_l are displayed in Fig. S8(a). The UV pulse interaction with the gold surface creates a transient hot electron population with T_e rising up to 1750 K. The electron system's temperature T_e nevertheless rapidly decreases as the hot electrons diffuse into the substrate and scatter with the lattice's phonons. Upon this action, the latter's temperature T_l rises by about 15 K in 4 ps. It is noteworthy that neither temperature profile matches directly the delay-dependent ΔV_2 traces (Fig. S60.

The reflectivity change $\Delta R/R_0$ due to temperature-dependent Drude-like intraband transitions has been modeled according to Block *et al.* (main text and supplementary materials).[20] The simulations results are presented in Fig. S9 with the evolution as function of delay in (a) and as a function of second pump energy in (b). We note from (a) that the general time-dependent $\Delta R/R_0$ trace is similar to T_e in Fig. S8(a). Also, $\Delta R/R_0$ is much larger at lower energies, as can be expected from intraband transitions.

Similarly, we have computed the change in Fermi-Dirac (FD) electron distribution ($\Delta f/f_0$) as a function of temperature (Fig. S10). In order to relate $\Delta f/f_0$ to the optical response due to

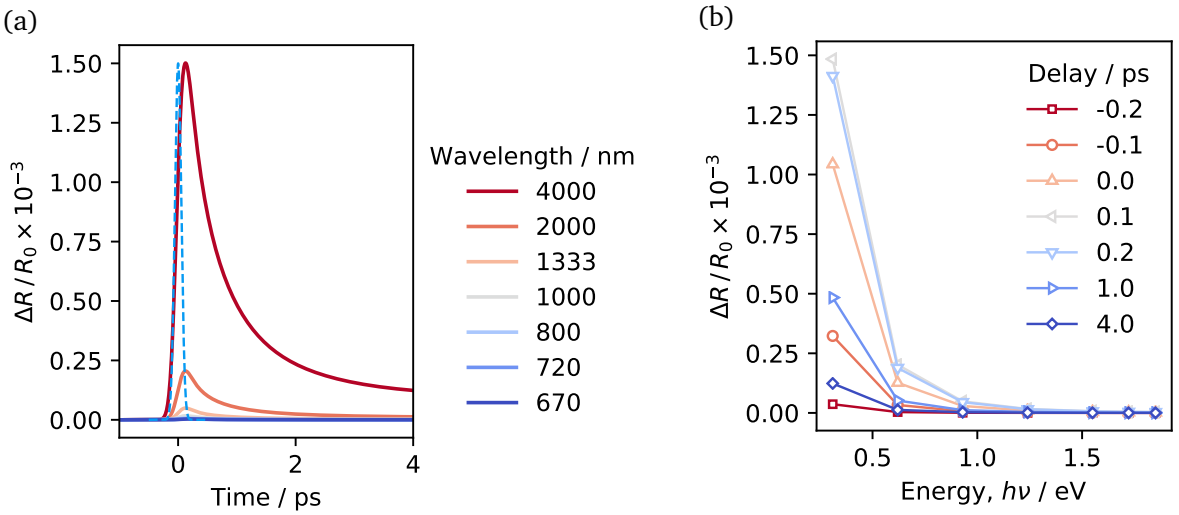

Figure S9: Calculated change in reflectivity due to intraband transitions in gold. (a) As a function of delay time. (b) As a function of photon energy for selected delay times.

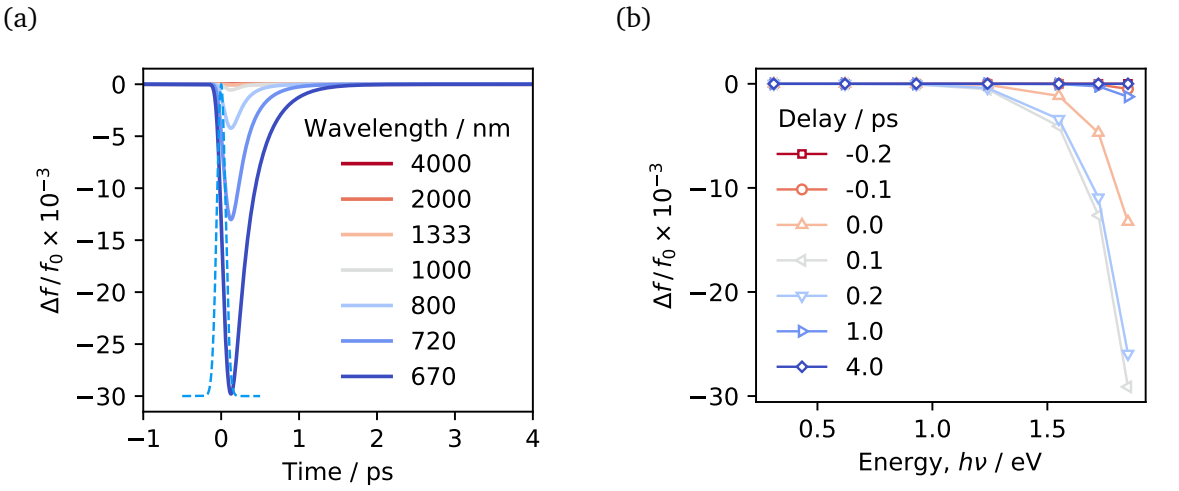

Figure S10: Calculated change (smearing) in Fermi-Dirac electron distribution in gold due to a perturbation by a UV pulse. (a) As a function of delay time for given wavelengths. (b) As a function of photon energy for selected delay times.

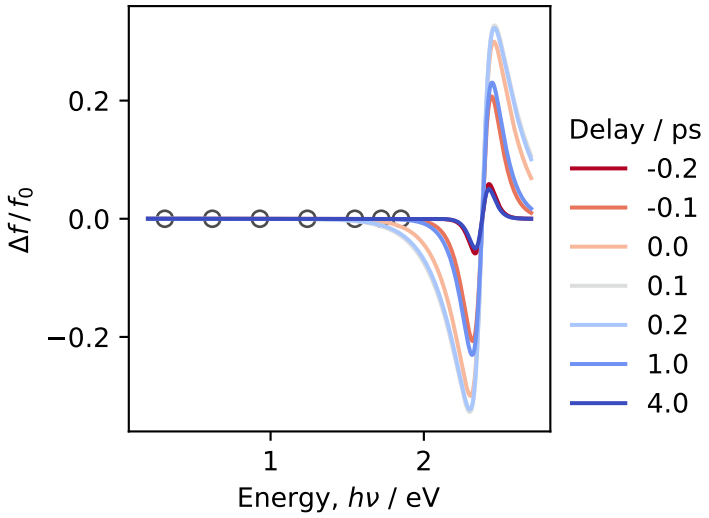

Figure S11: Calculated change (smearing) in Fermi-Dirac electron distribution in gold due to a perturbation by a UV pulse for a broad range of photon energy. The circles show the position, in energy, of this study's data.

interband transitions, a detailed knowledge of gold's complex permittivity in the k-space would be necessary. Nevertheless, the interband transition probability should be dependent on the FD electron distribution and we use here the readily available $\Delta f/f_0$ parameter to represent the temporal changes in the system. From Fig. S10(a), we can see that $\Delta f/f_0$ rapidly increases upon excitation, but decays almost as fast. In this case, the larger change can be seen at higher energies [Fig S10(b)]. Fermi smearing is indeed maximal just above and below the interband threshold ($\sim$2.38 eV), yielding the typical "first derivative" shape (Fig. S11).

S-6 Discussion

S-6.1 Nature of the photovoltage ΔV_2

We discuss here four hypotheses for the origin of the photovoltage ΔV_2 and we expose arguments to rule out the first three: *i.* further photoinjection from the electrode, *ii.* photoejection of carriers from the aqueous interface to the electrode, iii. heat originating at the metal surface *via* metal's electronic system excitation, and *iv.* heat generated at the aqueous side of the interface *via* resonant absorption by interfacial species.

i. In the first hypothesis, we consider the possibility of injecting more electrons in the electrolyte from the population of hot electrons in the electrode through the action of the second laser pulse. However, this effect would follow the relaxation dynamics of hot nonequilibrium electron population in gold, which thermalization time is about 1 ps[19]. The expected dynamics thus do not correspond to the observations where a long-lasting signal persists up to 100 ps.

ii. The second hypothesis addresses the reverse process of *i.*, namely the photon-triggered return of hot carriers from the electrolyte interface to the electrode, in analogy to charge transfer inverse photoemission spectroscopy (CTRIPS). This possibility can be ruled out because the depletion from the EDL of carriers of the same charge as those photoinjected in the first place would mark a reversal of sign of the photovoltage deltas. Yet, the observations show ΔV_2, induced by the second pump, to be of the same sign as ΔV_1 which is caused by the first pump.

iii. The third hypothesis assumes that the elevated temperature of the metal electrode surface induces a change in the metal absorptivity that increases the amount of heat generated upon excitation with the second pump. This change in metal absorptivity can come from the perturbation of three types of optical transitions: intraband transitions, normal interband transitions, and low energy interband transitions. Firstly, elevated T_e and T_l modify the reflectivity related to intraband transitions through an increase of the effective electron scattering rate and decrease of the free carrier density [see Fig. S9(a) and (b)].[20] Temperature-induced changes in intraband transitions affect mainly the lower energy portion of the spectrum, with a monotonous decrease towards higher energy; a Drude-like model does not afford any mechanism to account for a shoulder appearing at higher energy. Moreover, the expected dynamics of the intraband contributions is a sharp initial transient due to the nonequilibrium hot electron population, and a persisting signal due to the long-lasting effect of the heat transferred to the lattice (T_l). To the contrary, our observations show a rapid rise and fall of the signal at 0.31 and 0.62 eV, with no residual after $\sim$500 fs [Fig. 1(b), main text]. Secondly, perturbation of the normal interband transitions of gold results in a differential spectral shape reflecting the change of electron occupancy.[21] The electron occupancy change is itself described by the Fermi smearing induced by the first excitation pump [see Fig S10(a) and (b)]. Fermi smearing, however, can not explain the sloping of the spectra from the infrared to the visible, nor the presence of a shoulder at 1.55 eV [Fig. 1(d), main text]. Nevertheless, the reversal of the sloping of the spectra at short delays [blue to red traces, Fig. 1(d),

main text] in comparison to the spectra at longer delays cannot be explained by Fermi smearing, in which case a smooth decay of the signal concomitant with a shift towards higher energy would be expected. We instead observe a signal that seems to peak in the THz region and traverses the measurement range to settle in the visible region. Thirdly, depletion of the metal valence states opens the possibility of *low energy* interband transitions from the *d* band to the *s* band. The spectral response of these low energy interband transitions should evolve inversely to the intraband transitions, where the lower energy transitions will be quenched before the higher energy ones due to the energy dependence of the electron-electron scattering time[22]. We have not been able to rule out this possible contribution to the signal, nor the concurrent evolution of intraband and normal interband transitions. A proper modeling of the gold dielectric function response to an excitation pulse with respect to time would be required to understand their contribution. While it is not possible to rule out this possible contribution to the signal, no previous studies have shown metal dynamics similar to Fig. 1(d) (main text). Furthermore, as discussed above, replacing the 267 nm first pump with a 400 nm pump completely quenches the ultrafast response at the interface [Fig. 2(b), main text]. Relatedly, the contribution of a surface plasmon resonance (SPR) can also be ruled out since gold's SPR is found around 600 nm and, due to momentum conservation, it cannot be excited in free space in the far field. The resonance maximum of a localized surface plasmon resonance (LSPR) may be pushed to the near-infrared, but they appear in cases where the electronic wavefunction is confined, such as in nanoparticles, patterned surfaces or roughened surfaces. Moreover, here also, a possible plasmon contribution does not hold against the all-or-nothing experimental evidence provided by the switch from a 267 nm first pump to 400 nm. This behavior suggests the existence of an excitation threshold whose energy is higher than the SPR and interband transitions.

This leads to *iv.*, the resonant excitation of species present at the interface, resulting in an increase in the amount of heat generated at the metal/solution boundary. In bulk water, the excess electron frequency-dependent dynamics are characterized by a high energy absorption band centered around 1.72 eV (720 nm) and by a low energy absorption band peaking in the terahertz region. As discussed in § S-1, a change in the metal-solution boundary temperature produces a potential difference between the electrodes.

S-6.2 Effective spectra

The spectrum a_2 [top panel of Fig. 4(c), main text] corresponding to the hot electron population shows a profile that rises strongly at low energies. It can be best fitted by a Lorentzian peak shape centered at 0 with a full width at half maximum (FWHM) of (0.2 ± 0.1) eV. With the *caveat emptor* that the sparse data prevents us from reaching a definitive conclusion about the peak shape and position, we chose to use a Lorentzian function to model the a_3 spectrum and a Gaussian function to model the a_4 spectrum. The position of the maximum, the physical parameter we aim to obtain through the fit, is anyway insensitive to the actual model because of the low spectral resolution. The modelling of the spectrum of the trapped electron population a_3 [middle panel of Fig. 4(c), main text] with a Lorentzian function yielded a center energy of (1.51 ± 0.03) eV with a FWHM of (0.31 ± 0.05) eV. Similarly, fitting the spectrum of the solvated electron population a_4 [bottom panel of Fig. 4(c), main text] gave a center position of (1.47 ± 0.02) eV and a FWHM of (0.27 ± 0.03) eV for the Gaussian function.

S-6.3 Local concentration in the Helmholtz layers

According to the Gouy-Chapman-Stern model, in the absence of specific adsorption, the inner Helmholtz layer (IHL) of the interface will be covered by water molecules. If we assume the outer Helmholtz layer (OHL) of the interface is occupied by a monolayer containing an equal number of solvated cations and anions, the maximum local concentration of the cations (which have been shown to play more roles in interacting with solvated electron than anions) can be estimated as following: It is known that, in a 0.5 M Na_2SO_4 solution, the molar ratio between Na^+ and H_2O is 1:56. If we assume one ion is solvated by 4-6 water molecules, the ratio of the total number of cations and water molecules (including the IHL's water molecules and those solvating the SO_4^{2-} ions) is roughly 1:10, which gives a concentration of about 6 M for Na^+ at the interface.

S-6.4 Comparison with CTTS and 2PPE measurements

In charge transfer to solvent (CTTS) experiments[23], an electron-rich anion (typically an halide, such as I^- [23,24], Cl^- [25], etc., or a ferrocyanide[26]) is excited using single or multiphoton absorption. The excited electron gets bound to a CTTS state created by the potential well due to solvent

polarization around the now neutral atom or molecule as the solvent molecules did not have the time to reorganize. Reorientation of the solvent molecules in the surroundings of the CTTS state destroys this state and separates the electron from the neutral particle.[27] The electron is thus found in a solvated state that is basically a modified ground state with *s* symmetry. Multiphoton absorption (more energetic pump) could also lead to ionization by promoting the electron directly to a continuum of states that can transfer to the water conduction band. The latter has more similarities with multiphoton ionization of neat water.

In our experiments, there is no strong incentive to believe that a true analog to a CTTS state is formed. The first UV pump has enough energy to provoke the emission from the hot excited states in the metal to the water conduction band. In fact, this process is more similar to the multiphoton ionization of water[28,29] because a transient hole is left behind in the metal which necessarily interacts with the electron through Coulombic forces. In analogy, the electron interacts with the H_2O^+ ion in the water ionization process. In our experiment, in contrast to the multiphoton ionization of water, it is known from gold ultrafast dynamics that the transient hole is effectively screened on a time scale of a few femtoseconds[30].

We must also distinguish between studies that follow the relaxation of electrons following generation (right after photodetachment or photoionization) and the relaxation of electrons excited from an equilibrated solvated state.[27] Our experiment is more similar to the former case.

Our experiment bears obvious similarities with the two-photon photoelectron spectroscopy (2PPE) technique on metal surfaces where photoemission is used to inject excess electrons in an amorphous ice layer,[31] whereas the detection method differs. In that regard, some level of coupling of the excess electrons to the substrate[32] can be expected, which is a plausible explanation for the transformation from state S_3 to state S_4.

In summary, photoinjection from a metal electrode is an intermediate approach with its own particularities, which shares features with CTTS and multiphoton ionization of water, and which parallels the mechanism for excess electron generation from 2PPE. In this specific case, the UV photon has enough energy to excite an electron from gold's Fermi level to water's conduction band. A transient hole persists in the metal for a few femtoseconds. During this brief time the ejected electron is subjected to Coulombic interaction with the transient hole. Upon cooling down,

our measurements show that the electron finds a preexisting trap in the interfacial water layer. Follows a rearrangement of the water molecules around the electron as described in the main text.

References

[1] Richardson, J. H.; Deutscher, S. B.; Maddux, A. S.; Harrar, J. E.; Johnson, D. C.; Schmelzinger, W. L.; Perone, S. P. Laser-Induced Photoelectrochemistry: Coulostatic Measurements of Photoemission in Aqueous and Non-Aqueous Solutions. *J. Electroanal. Chem. Interfacial Electrochem.* **1980**, *109*, 95–114.

[2] Gurevich, Y. Y.; Pleskov, Y. V.; Rotenberg, Z. A. *Photoelectrochemistry*; Springer US: Boston, MA, 1980.

[3] Benderskii, V. A.; Velichko, G. I. Temperature Jump in Electric Double-Layer Study. Part I. Method of Measurements. *J. Electroanal. Chem.* **1982**, *140*, 1–22.

[4] Smalley, J. F.; Krishnan, C. V.; Goldman, M.; Feldberg, S. W.; Ruzic, I. Laser-Induced Temperature-Jump Coulostatics for the Investigation of Heterogeneous Rate Processes. Theory and Application. *J. Electroanal. Chem.* **1988**, *248*, 255–282.

[5] Scott, T. W. Picosecond Photoemission and Recombinatlon Dynamics at the Metal-Liquid Interface. *J. Phys. Chem.* **1986**, *90*, 1739–1741.

[6] Smalley, J. F.; Geng, L.; Feldberg, S. W.; Rogers, L. C.; Leddy, J. Evidence for Adsorption of $Fe(CN)_6^{3-/4-}$ on Gold Using the Indirect Laser-Induced Temperature-Jump Method. *J. Electroanal. Chem.* **1993**, *356*, 181–200.

[7] Climent, V.; Coles, B. A.; Compton, R. G. Laser Induced Current Transients Applied to a Au(111) Single Crystal Electrode. A General Method for the Measurement of Potentials of Zero Charge of Solid Electrodes. *J. Phys. Chem. B* **2001**, *105*, 10669–10673.

[8] Pope, R. M.; Fry, E. S. Absorption Spectrum (380–700 nm) of Pure Water. II. Integrating Cavity Measurements. *Appl. Opt.* **1997**, *36*, 8710–8723.

[9] Curcio, J. A.; Petty, C. C. The Near Infrared Absorption Spectrum of Liquid Water. *J. Opt. Soc. Am.* **1951**, *41*, 302–304.

[10] Downing, H. D.; Williams, D. Optical Constants of Water in the Infrared. *J. Geophys. Res.* **1975**, *80*, 1656–1661.

[11] Polyanskiy, M. N. Refractive Index Database. https://refractiveindex.info, (accessed Aug 15, 2019).

[12] Diels, J. C.; Rudolph, W. In *Ultrashort Laser Pulse Phenomena*, 2nd ed.; Liao, P. F., Kelley, P., Eds.; Academic Press, Inc.: Burlington, 2006.

[13] The Effect of Dispersion on Ultrashort Pulses (Newport). https://www.newport.com/n/the-effect-of-dispersion-on-ultrashort-pulses, (accessed Aug 15, 2019).

[14] Alber, L.; Valentino, S.; Vivek, U.; Stefano, B. udcm-su/heat-diffusion-1D: NTMpy-package. 2019; https://zenodo.org/record/3333493, DOI: 10.5281/ZENODO.3333493.

[15] Eesley, G. L. Generation of Nonequilibrium Electron and Lattice Temperatures in Copper by Picosecond Laser Pulses. *Phys. Rev. B* **1986**, *33*, 2144–2151.

[16] Smith, A. N.; Norris, P. M. Influence of Intraband Transitions on the Electron Thermoreflectance Response of Metals. *Appl. Phys. Lett.* **2001**, *78*, 1240–1242.

[17] Jain, A.; McGaughey, A. J. Thermal Transport by Phonons and Electrons in Aluminum, Silver, and Gold from First Principles. *Phys. Rev. B* **2016**, *93*, 081206(R).

[18] Stähler, J.; Deinert, J.-C.; Wegkamp, D.; Hagen, S.; Wolf, M. Real-Time Measurement of the Vertical Binding Energy During the Birth of a Solvated Electron. *J. Am. Chem. Soc.* **2015**, *137*, 3520–3524.

[19] Fann, W. S.; Storz, R.; Tom, H. W. K.; Bokor, J. Electron Thermalization in Gold. *Phys. Rev. B* **1992**, *46*, 13592–13595.

[20] Block, A.; Liebel, M.; Yu, R.; Spector, M.; Sivan, Y.; García de Abajo, F. J.; van Hulst, N. F. Tracking Ultrafast Hot-Electron Diffusion in Space and Time by Ultrafast Thermomodulation Microscopy. *Sci. Adv.* **2019**, *5*, eaav8965.

[21] Schoenlein, R. W.; Lin, W. Z.; Fujimoto, J. G.; Eesley, G. L. Femtosecond Studies of Nonequilibrium Electronic Processes in Metals. *Phys. Rev. Lett.* **1987**, *58*, 1680–1683.

[22] Sun, C.-K.; Vallée, F.; Acioli, L.; Ippen, E. P.; Fujimoto, J. G. Femtosecond Investigation of Electron Thermalization in Gold. *Phys. Rev. B* **1993**, *48*, 365–368.

[23] Kloepfer, J. A.; Vilchiz, V. H.; Lenchenkov, V. A.; Germaine, A. C.; Bradforth, S. E. The Ejection Distribution of Solvated Electrons Generated by the One-Photon Photodetachment of Aqueous I^- and Two-Photon Ionization of the Solvent. *J. Chem. Phys.* **2000**, *113*, 6288–6307.

[24] Long, F. H.; Shi, X.; Lu, H.; Eisenthal, K. B. Electron Photodetachment From Halide Ions in Solution: Excited-State Dynamics in the Polarization Well. *J. Phys. Chem.* **1994**, *98*, 7252–7255.

[25] Assel, M.; Laenen, R.; Laubereau, A.; Resolution, P. Dynamics of Excited Solvated Electrons in Aqueous Solution Monitored with Femtosecond-Time and Polarization Resolution. *J. Phys. Chem. A* **1998**, *102*, 2256–2262.

[26] Pommeret, S.; Naskrecki, R.; van der Meulen, P.; Ménard, M.; Vigneron, G.; Gustavsson, T. Ultrafast Events in the Electron Photodetachment From the Hexacyanoferrate(II) Complex in Solution. *Chem. Phys. Lett.* **1998**, *288*, 833–840.

[27] Vilchiz, V. H.; Kloepfer, J. A.; Germaine, A. C.; Lenchenkov, V. A.; Bradforth, S. E. Map for the Relaxation Dynamics of Hot Photoelectrons Injected into Liquid Water via Anion Threshold Photodetachment and Above Threshold Solvent Ionization. *J. Phys. Chem. A* **2001**, *105*, 1711–1723.

[28] Migus, A.; Gauduel, Y.; Martin, J. L.; Antonetti, A. Excess Electrons in Liquid Water: First Evidence of a Prehydrated State with Femtosecond Lifetime. *Phys. Rev. Lett.* **1987**, *58*, 1559–1562.

[29] Savolainen, J.; Uhlig, F.; Ahmed, S.; Hamm, P.; Jungwirth, P. Direct Observation of the Collapse of the Delocalized Excess Electron in Water. *Nat. Chem.* **2014**, *6*, 697–701.

[30] Cui, X.; Wang, C.; Argondizzo, A.; Garrett-Roe, S.; Gumhalter, B.; Petek, H. Transient Excitons at Metal Surfaces. *Nat. Phys.* **2014**, *10*, 505–509.

[31] Gahl, C.; Bovensiepen, U.; Frischkorn, C.; Wolf, M. Ultrafast Dynamics of Electron Localization and Solvation in Ice Layers on Cu (111). *Phys. Rev. Lett.* **2002**, *89*, 107402.

[32] Stähler, J.; Gahl, C.; Bovensiepen, U.; Wolf, M. Ultrafast Electron Dynamics at Ice-Metal Interfaces: Competition Between Heterogeneous Electron Transfer and Solvation. *J. Phys. Chem. B* **2006**, *110*, 9637–9644.